



Characteristics of high-rank coal structure parallel and perpendicular to the bedding plane via NMR and X-ray CT

Shi-Qi Liu^{1,2} · Shu-Xun Sang^{3,4} · Qiu-Jia Hu⁵ · Hui-Huang Fang^{3,4}

Received: 8 August 2019
© The Author(s) 2020

Abstract

Pores and fractures and their connectivity play a significant role in coalbed methane production. To investigate the growth characteristics and connectivity of pores and fractures in coal parallel and perpendicular to the bedding plane, the pores and fractures of high-rank coal samples collected from the southern Qinshui Basin were measured by low-field nuclear magnetic resonance, X-ray-computed tomography and field emission scanning electron microscopy. Then, the determinants of their connectivity were further discussed. The results show that the high-rank coal samples have similar pore size distributions both parallel and perpendicular to the bedding plane. They primarily contain mesopores (2–50 nm in width), followed by macropores (> 50 nm in width). The research indicated that the high-rank coal connectivity parallel to the bedding plane is significantly better than that perpendicular to the bedding plane. The connectivity of high-rank coal is mainly determined by throats, and the orientation of the pores and fractures. The two connectivity modes in high-rank coal are “pore connectivity,” in which the throats are mainly pores with a low coordination number, and “microfissure connectivity”, in which the throats are mainly microfissures with a high coordination number.

Keywords Porosity · Connectivity · Pore width · Microfissure · High-rank coal · Qinshui Basin

1 Introduction

Pores in coal are the main spaces for coalbed methane (CBM) storage, while fractures are the main channel for gas and water flow (Liu et al. 2015, 2018a). The pore structure,

e.g., porosity, scale, morphology and connectivity, plays a key role in CBM production (Liu et al. 2015, 2018a; Lai et al. 2016, 2018). The pores in coal are generally classified into four categories, i.e., primary pores, epigenetic pores, coalification-related pores and mineral-related pores (Chen et al. 2015; Lai et al. 2016, 2018; Liu et al. 2017). The genesis and morphology of the pores are closely related to the microlithotype, metamorphism and deformation of the coal (Alexeev et al. 2007; Zhang et al. 2010, 2018; Zhu et al. 2016; Li et al. 2018). The pores in coal directly impact gas generation, gas accumulation and coal permeability, and control the adsorption, diffusion and seepage of CH₄ in coal (Alexeev et al. 2007; Zhang et al. 2010; Zhu et al. 2016; Du et al. 2019). Fractures are the main channel for fluid migration and output and are the key factor for coal permeability (Yao et al. 2010a; Liu et al. 2016). Fractures can be divided into macroscopic fractures and microscopic fractures (Chen et al. 2015; Lai et al. 2017; Zhang et al. 2017; Zhou et al. 2018). Microscopic fractures can be further divided into endogenous fractures and exogenous fractures (Chen et al. 2015; Zhang et al. 2017; Zhou et al. 2018). Fractures are generally believed to form from internal forces and external forces (Yao et al. 2010b; Li et al. 2014; Liu et al. 2016).

Edited by Jie Hao and Xiu-Qiu Peng

✉ Shu-Xun Sang
shxsang@cumt.edu.cn

- ¹ Low Carbon Energy Institute, China University of Mining and Technology, Xuzhou 221008, China
- ² Jiangsu Key Laboratory of Coal-based Greenhouse Gas Control and Utilization, China University of Mining and Technology, Xuzhou 221008, China
- ³ School of Mineral Resource and Geoscience, China University of Mining and Technology, Xuzhou 221116, China
- ⁴ Key Laboratory of Coalbed Methane Resources and Reservoir Formation Process, Ministry of Education, China University of Mining and Technology, Xuzhou 221008, China
- ⁵ Shanxi CBM Branch of Huabei Oilfield Company, China National Petroleum Corporation, Jincheng 048000, China

Tectonic evolution, metamorphism and microlithotype play a key role in the formation of fractures (Yao et al. 2010a; Li et al. 2014; Liu et al. 2016; Ai et al. 2018).

Research on pores and fractures is focused on their morphology, genetic type, scale, syntagmatic relation, connectivity, and their relationships with coal porosity and permeability, fluid occurrence, migration and output (Liu et al. 2016, 2017; Li et al. 2017, 2019). Characteristics of the coal structure parallel and perpendicular to the bedding plane are rarely considered. For vertical CBM wells, the fluid flow in coal can be regarded as radial fluid flow; thus, fluid migration perpendicular to the bedding plane can be ignored, and the coal structure, connectivity and permeability in this orientation can also be disregarded (Clarkson and Bustin 1999; Wei et al. 2007; Aminian and Ameri 2009). However, during horizontal CBM well production, fluid flow is mainly sphere-shaped flow in the horizontal section; thus, fluid migration perpendicular to the bedding plane cannot be ignored, and the coal structure, connectivity and permeability in this orientation are important to CBM production (Keim et al. 2011; Wen et al. 2011; Fang et al. 2019). Therefore, the investigation of the growth characteristics and connectivity of pores and fractures in coal parallel and perpendicular to the bedding plane is significant to horizontal CBM well production and can provide a better understanding of fluid migration in coal.

Pores and fractures in coal are mainly studied by traditional methods, e.g., optical microscopy, electron microscopy, mercury intrusion porosimetry and nitrogen/CO₂ adsorption tests (Bolin 2014; Okolo et al. 2015). These traditional methods have limitations, e.g., difficulty in studying pore-fracture connectivity and the destruction of pores and fractures during sample preparation and testing (Okolo et al. 2015; Liu et al. 2018a). Nuclear magnetic resonance (NMR) and X-ray computed tomography (CT) scanning are becoming important technologies to study pores and fractures in coal due to their measurement speed and nondestructive testing (Mathews et al. 2011; Yao and Liu 2012; Smolná et al. 2013; Zhao et al. 2017). In this paper, an integrated approach combining low-field nuclear magnetic resonance (LF-NMR), X-ray CT, and field emission scanning electron

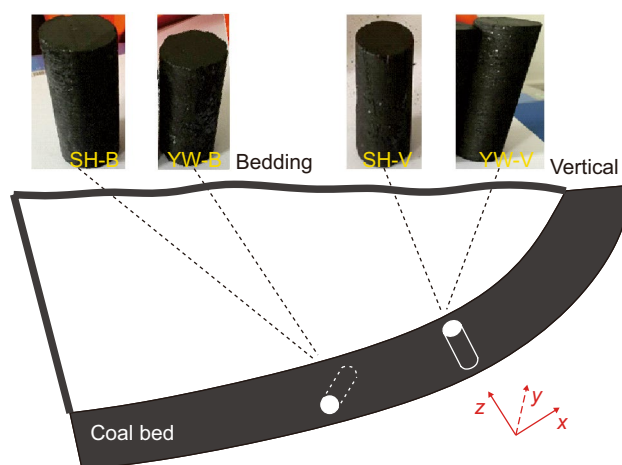


Fig. 1 Sketch map of coal sample preparation. Modified from Liu et al. (2018b)

microscopy (FESEM) was employed to describe the coal porosity, pore size distribution, genetic types, and connectivity parallel and perpendicular to the bedding plane, and the reasons for the differences in connectivity between the two orientations were further explained. This study aims to provide a better understanding of fluid migration and output during horizontal CBM well production.

2 Materials and methodology

2.1 Sample

The two coal samples used in this study were systematically collected from coal seam #3 of the Shanxi Formation in the southern Qinshui Basin in China. Anthracite was collected from the Sihe Mine, and semi-anthracite coal was collected from the Yuwu Mine (Table 1). The coal samples were collected in large blocks (approximately 300 × 300 × 300 mm). The coal pillars used in the study were drilled parallel and perpendicular to the bedding plane for each coal sample (Fig. 1). Coal pillars with a diameter of approximately

Table 1 Physical properties of the coal samples used

Sample	Sample location	Ro, max, %	Proximate analysis, wt%				Sample parameters		
			M _{ad}	A _{ad}	V _{daf}	FC _{ad}	Drilling direction	Length, mm	Diameter, mm
SH-B	Sihe Mine	3.33	2.71	12.18	6.94	81.72	Bedding	53.5	24.3
SH-V							Vertical	57.6	24.6
YW-B	Yuwu Mine	2.96	1.48	13.12	6.32	81.39	Bedding	42.8	23.5
YW-V							Vertical	44.8	24.7

Ro, max, the mean maximum reflectance values of vitrinite; wt%, weight percent; M_{ad}, moisture; A_{ad}, ash yield; V_{daf}, volatile matter; FC_{ad}, fixed carbon; ad, air dried; daf, dry ash free

25 mm and a length of 40–60 mm were drilled by a mechanical drill, and their ends were polished with a grinder (Fig. 1). The names, key properties and sizes of these coal pillars are shown in Table 1.

2.2 LF-NMR

2.2.1 LF-NMR analyzer

The NMR experiment was performed with a MicroMR12-025 V LF-NMR analyzer made by Suzhou Niumag Analytical Instrument Corporation, China. The resonance frequency of the LF-NMR analyzer is 11.897 MHz, and the magnet temperature is 1.99–32.01 °C.

2.2.2 LF-NMR experimental process

- A. The coal pillars were first vacuum dried at 50 °C for 24 h and then immediately saturated with distilled water for more than 24 h.
- B. LF-NMR experiments on 100% water-saturated coal pillars were carried out to obtain T_2 (the transverse relaxation time, ms) spectra under 100% water-saturated conditions (S_w).
- C. Then, the coal pillars were centrifuged at a high speed using a centrifugal pump at 200 Psi for 1.5 h to achieve irreducible water conditions (S_{ir}).
- D. LF-NMR experiments on coal pillars at S_{ir} were carried out to obtain T_2 spectra at S_{ir} .

2.2.3 T_2 spectra analysis

A. Effective porosity

The NMR signals of coal pillars at S_w can be measured and scaled using a standard sample. Then, NMR signals can be converted to porosity using Eq. 1.

$$\varphi = \Phi \cdot \frac{s}{S} \cdot \frac{N_s}{n_s} \cdot 10^{\frac{1}{20}(RG1-rg1)} \cdot 2^{(RG2-rg2)} \quad (1)$$

where Φ , $RG1$, $RG2$ and S are the porosity, simulation gain, signal strength and NMR signal value of the standard sample, respectively; φ , n_s , $rg1$, $rg2$, and s are the porosity, cumulative collection time, simulation gain, signal strength and NMR signal value of the coal pillars, respectively.

The effective porosity (φ_{pr} , also called producible porosity, %) is obtained by the cumulative T_2 spectra method proposed by Yao et al. (Yao et al. 2014; Zhao et al. 2017). The maximum peak amplitudes of cumulative T_2 spectra at S_w and S_{ir} are equal to cumulative porosity at S_w (φ_w , %) and S_{ir} (φ_{ir} , also called irreducible porosity, %), respectively. φ_{pr} is the difference between the φ_w and φ_{ir} .

B. Pore size distribution

The “ T_2 cutoff value” (T_{2C} is the threshold for φ_{pr} and φ_{ir} , ms) is used to calculate the pore size distribution of the coal samples. Assuming that the pore radius (r) corresponding to T_{2C} is constant for all coal samples, the pore radius (r_{ci}) corresponding to i relaxation time (T_{2i}) can be expressed as Eq. 2 (Yao and Liu 2012; Yao et al. 2014).

$$r_{ci} = r \frac{T_{2i}}{T_{2C}} \quad (2)$$

In this study, the pore radius corresponding to the T_{2C} was chosen to be 0.1 μm .

2.3 Three-dimensional (3D) coal structure modeling

2.3.1 X-ray CT scanning

X-ray CT scanning was performed by the X-ray CT scanner Xradia 520 Versa produced by the Carl Zeiss Foundation Group, Germany. The X-ray CT scanning samples were small coal pillars of approximately 2 mm in diameter and 2 mm in height (Fig. 2). The samples were drilled using a mechanical sampler.

The X-ray CT scanning area was 2 mm in diameter and 1 mm in height. The total of 3600 scans were performed at a spatial resolution of 1 μm . X-ray CT scanning provides structural information for the development of a 3D pore-fracture network model of the coal samples at a cubic scale of approximately 400 μm on each side. The process of establishing the 3D pore-fracture network model using the X-ray CT scanner includes several steps, and threshold selection is the key to identifying pores and fractures during this process. The distribution intervals of the thresholds for minerals, organic matter and pore fractures were 3000 Hounsfield units (HU), 1000–1800 HU and < 600 HU, respectively (Yao et al. 2010a).

2.3.2 3D pore-fracture network modeling

A 3D pore-fracture network model is established via Avizo 9, which is professional software used to produce a 3D digital core using 3D X-ray CT scanning images. The main steps include skeletonization of the pore-fracture space, description of the pore-fracture system, segmentation of the pore-fracture space, establishment of a new 3D pore-fracture network model and analysis of the spatial structure parameters. The process of establishing the 3D pore-fracture network model is beyond the scope of this paper, and the details can be referenced elsewhere (Hughes and Blunt 2001; Knackstedt et al. 2005; Ma et al. 2014a, b).

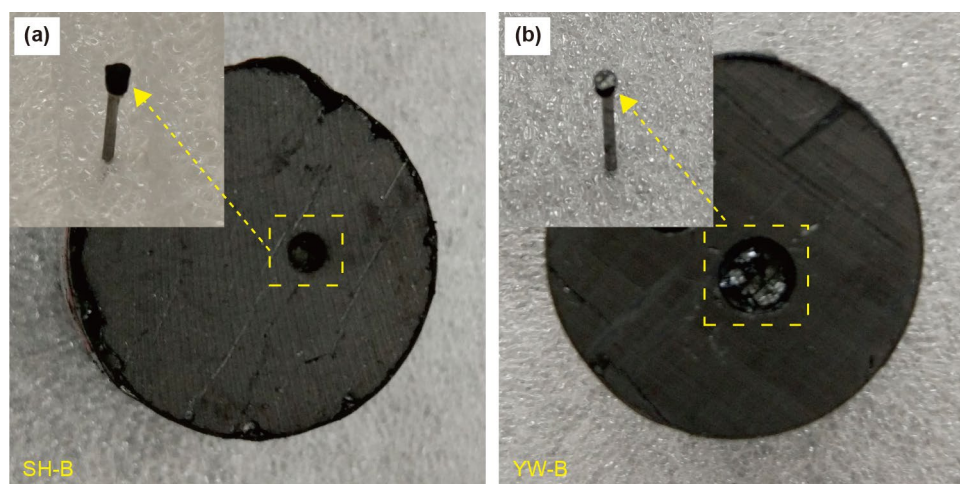


Fig. 2 Photographs of coal samples for X-ray CT

2.4 Scanning electron microscopy analysis

Pores, fractures and minerals were investigated using an FESEM SUPRA 55 produced by the Carl Zeiss Foundation Group, Germany, with amplification from 10^3 to 10^5 . Bulk coal samples were analyzed by FESEM. The coal samples were polished into small lumps approximately 10 mm across and 2–3 mm high using a polishing and burnishing machine. Then, the small lumps of coal were polished using a cross-section polisher. Coal is known as a nonconducting substance. Therefore, to achieve better experimental results, coal samples were usually spluttered with a thin gold coating. The pores were observed using the high-vacuum mode.

3 Results

3.1 Porosity of the coal samples

According to the NMR results, the development and connectivity of the pores in the Sihe coal samples are better than those in the Yuwu coal samples. The φ_N , φ_w , φ_{ir} and φ_{pr} of the Sihe coal samples are higher than those of the Yuwu coal

samples, where the φ_N of the Sihe coal samples is approximately 2 times that of the Yuwu coal samples (Table 2). The φ_N and φ_{ir} of the coal samples parallel to the bedding plane are lower than those perpendicular to the bedding plane, whereas the φ_w and φ_{pr} of the coal samples parallel to the bedding plane are higher than those perpendicular to the bedding plane (Table 2). This finding indicates that the coal samples have better pore connectivity parallel to the bedding plane.

The X-ray CT results also show that the pore development in the Sihe coal samples is better than that of the Yuwu coal samples due to the higher pore volumes and porosities (Table 2). The porosity of coal SH-B is lower than that of coal SH-V, and the Yuwu coal samples are the opposite.

3.2 Pore size distribution of the coal samples

This study used a pore structure classification system proposed by the International Union of Pure and Applied Chemistry (IUPAC), classifying the pores into micropores (<2 nm in width), mesopores (2–50 nm in width) and macropores (> 50 nm in width) (Moore 2012; Liu et al. 2017).

Table 2 Porosity, effective porosity and other parameters based on NMR and X-ray CT

Sample	NMR					X-ray CT		
	φ_N	φ_w	φ_{ir}	φ_{pr}	T_{2c}	V_s	V_p	φ_p
SH-B	7.43	9.75	8.18	1.57	1.32	64,000,030	1,840,930	2.88
SH-V	7.97	9.63	8.84	0.79	2.16	64,000,050	2,968,750	4.64
YW-B	3.28	7.60	6.15	1.45	0.31	64,000,000	1,054,180	2.52
YW-V	3.40	6.78	6.75	0.03	0.57	63,999,979	1,610,190	1.65

φ_N , porosity based on NMR, %; V_s , volume of coal sample used for X-ray CT, μm^3 ; V_p , pore volume based on X-ray CT, μm^3 ; φ_p , porosity based on X-ray CT, %

3.2.1 Pore size distribution by LF-NMR

The Sihe and Yuwu coal samples have similar pore size distributions. Mesopores (48.21%–76.61%) are most abundant, followed by macropores (23.37%–49.38%) (Fig. 3). The pores widths of the coal samples are mainly in the range of 2–500 nm, and the pore volume percent decreases with increasing pore width (Fig. 3). The pore size distribution parallel to the bedding plane is also similar to that perpendicular to the bedding plane. Mesopores are the most abundant in both orientations, followed by macropores of 50–500 nm in width, with the smallest volume percent of macropores > 1 μm (Fig. 3). In particular, 76.61% of the pores in the coal YW-V are mesopores, and the volume percent of macropores > 1 μm in the coal samples perpendicular to the bedding plane are slightly higher than those in the samples parallel to the bedding plane, indicating that mesopores and macropores > 1 μm are more abundant perpendicular to the bedding plane.

3.2.2 Pore size distribution by X-ray CT

The X-ray CT results show that the number and volume of macropores > 1 μm in the Sihe coal samples are higher than those in the Yuwu coal samples (Fig. 4). The number of macropores > 1 μm in the coal samples perpendicular to the bedding plane are larger than that in the coal samples parallel to the bedding plane. The volumes of macropores 1 μm–6 μm and > 50 μm in width in coal SH-V are significantly greater than those in coal SH-B, while the volumes of macropores 6 μm–30 μm in width in coal SH-V are slightly lower (Fig. 4). The volumes of macropores 1 μm–4 μm in width in coal YW-V are significantly greater than those in coal YW-B (Fig. 4). The volumes of macropores > 4 μm in coal YW-V are lower than those in coal YW-B, and with increasing pore width, the differences between the pore

volumes of coal YW-B and coal YW-V become more significant (Fig. 4). Therefore, pores with smaller widths are more abundant in the coal samples perpendicular to the bedding plane, while microscopic fractures and pores with larger width are more abundant in the coal samples parallel to the bedding plane.

3.3 Connectivity of the pores and fractures

3.3.1 Pores and fractures identified by T_2 spectra

The mesopores, macropores and microscopic fractures can be identified based on the T_2 spectra at S_w (Yao et al. 2010a; Yao and Liu 2012). Coal SH-B and coal SH-V have similar T_2 spectra at S_w . Their T_2 spectra at S_w have three peaks consisting of two large peaks and one small peak (Fig. 5). The two large peaks located at 0.01–0.2 ms and 0.2–5.0 ms are the peaks of the most abundant pores, which represent pores with width ranges of 2–15 nm and 15–380 nm in coal SH-B, respectively, and represent pores with width ranges of 2–12 nm and 12–230 nm in coal SH-V, respectively (Fig. 5). The small peak is located at 20–100 ms (Fig. 5), which is the peak of the macropores > 1 μm, indicating that macropores > 1 μm are not abundant. In addition, the T_2 spectra at S_w of the Sihe coal samples lack peaks of microscopic fractures (Fig. 5), indicating that microscopic fractures are not abundant.

Similar to the Sihe coal samples, coal YW-B and coal YW-V also have similar T_2 spectra at S_w . Their T_2 spectra at S_w have one large peak and three small peaks (Fig. 5). The large peak is located at 0.02–1.0 ms and represents pores with width ranges of 10–300 nm in coal YW-B and 3.5–160 nm in coal YW-V (Fig. 5). The three small peaks are located at 2–25 ms, 25–500 ms and 500–1000 ms (Fig. 5), which are the peaks of macropores, microfissures and microfissures and cleats, respectively. The results show that microscopic fractures are abundant in the Yuwu coal

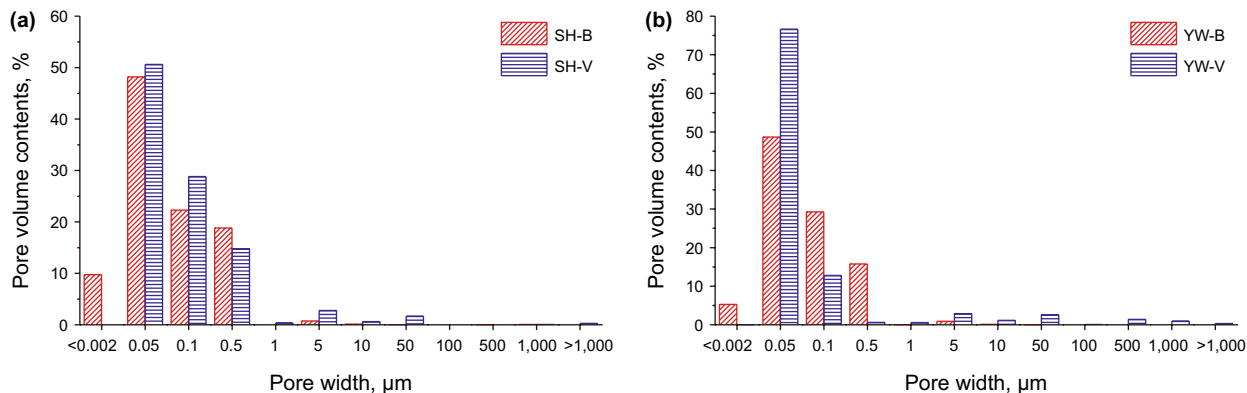


Fig. 3 Pore size distribution determined by NMR

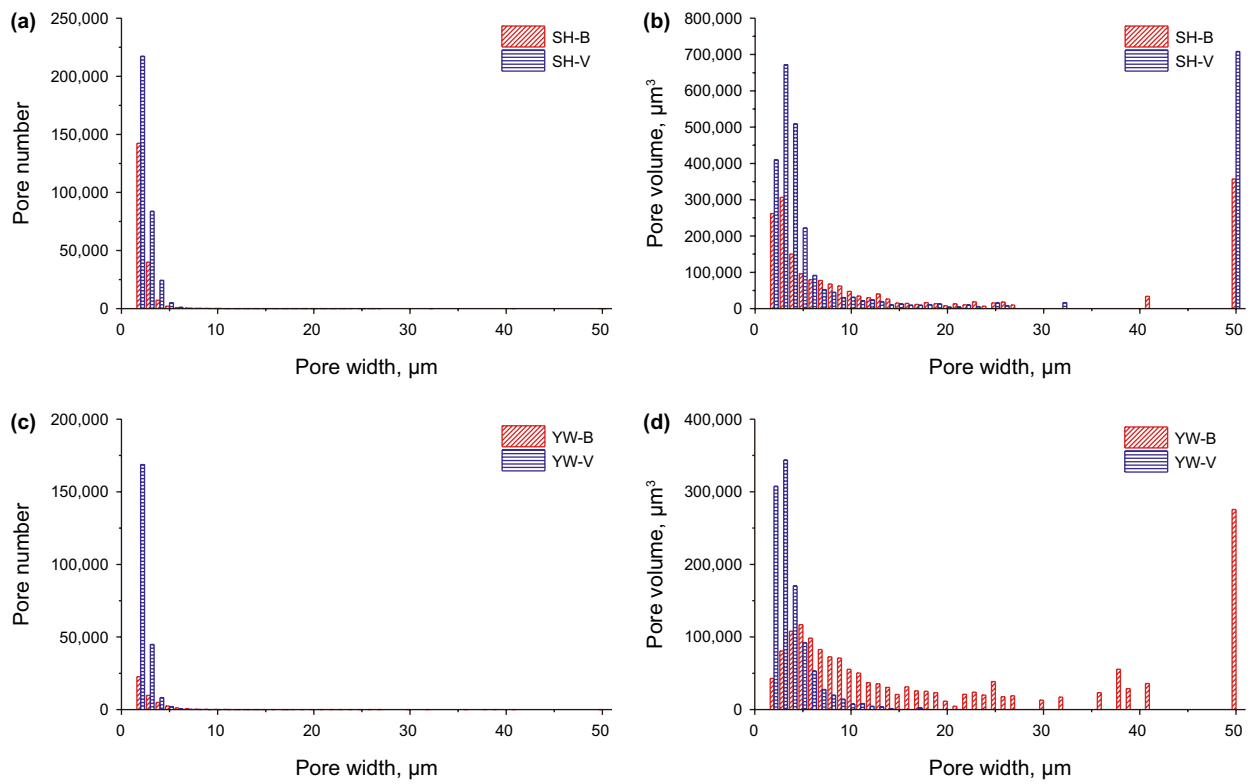


Fig. 4 Pore size distribution determined by X-ray CT

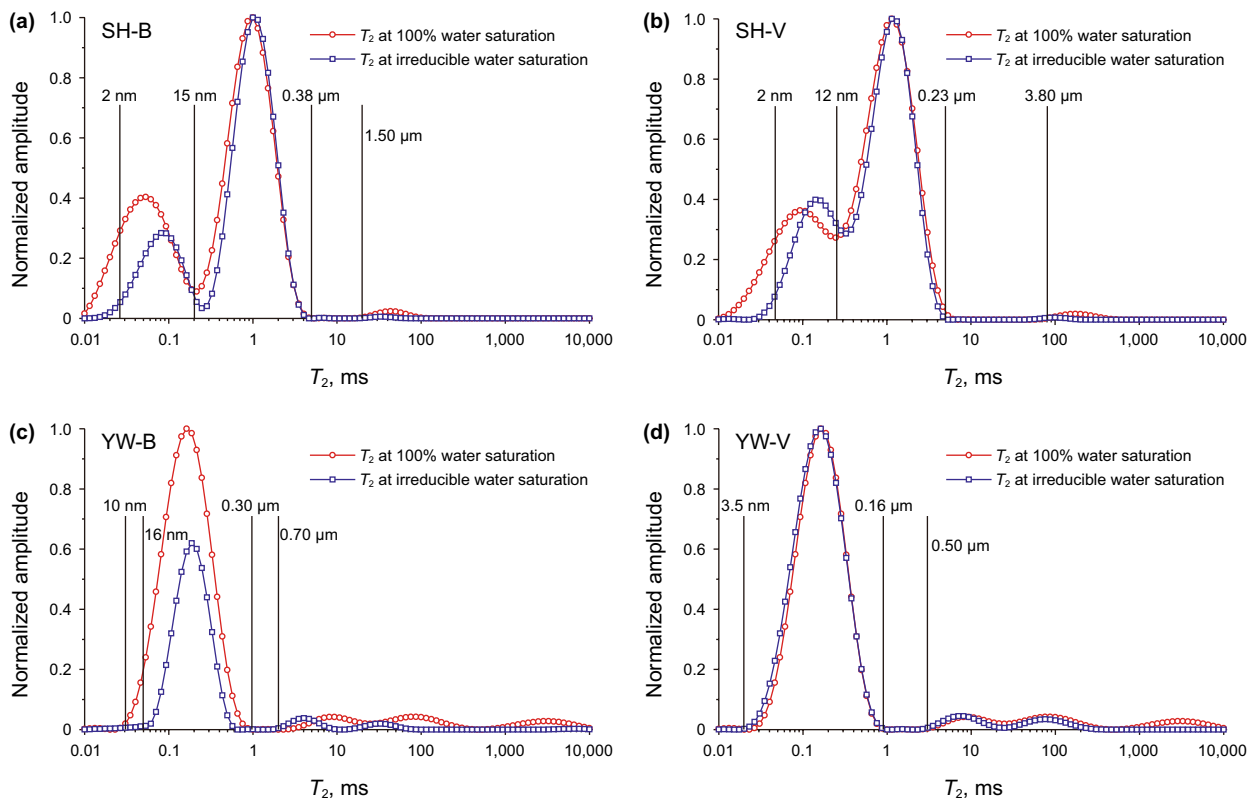


Fig. 5 NMR T_2 distribution

samples, which are related to the tectonic deformation of coal in the Yuwu Mine.

3.3.2 Connectivity of the pores and fractures by LF-NMR

By comparing the T_2 spectra at S_w and S_{ir} , the connectivity of the coal samples can be further analyzed (Yao et al. 2010a; Yao and Liu 2012). The peak of 0.01–0.2 ms in the Sihe coal samples has good continuity with the peak of 0.2–5.0 ms, indicating that pores with width ranges of 50–500 nm have good connectivity (Fig. 5). However, the peak of 0.2–5.0 ms is almost discontinuous with the peak of 20–100 ms due to the low number of pores $> 1 \mu\text{m}$ (Fig. 3). Coal SH-B has a different peak of 0.01–0.2 ms at S_{ir} for coal SH-V. The T_2 spectra at S_{ir} for SH-B is lower than those at S_w because of the good connectivity of the mesopores 2–15 nm allowing the water to be centrifuged. The T_2 spectra at S_{ir} for coal SH-B are significantly lower than those at S_w in the range of 0.01–0.1 ms and higher in the range of 0.1–0.2 ms (Fig. 5), because pores with widths of 2–12 nm have good connectivity, while the connectivity of pores with widths of 2–230 nm is poor. Under the centrifugal effects, the saturated water migrates from pores of 2–12 nm to larger-scale pores and accumulates in pores with widths of approximately 12 nm. Almost no change occurs between the T_2 spectra at S_{ir} and those at S_w for coal SH-V (Fig. 5). The connectivity of pores with widths of 12–230 nm is extremely poor, resulting in the connectivity and effective porosity of coal SH-V being lower than those of coal SH-B. The T_2 spectra at S_{ir} for coal SH-B are slightly higher than those at S_w in the range of 0.2–5.0 ms because of the low connectivity between pores of 15–380 nm and larger-scale pores. The migration of saturated water to larger-scale pores is difficult under the centrifugal effects. In addition, the small peak of macropores $> 1 \mu\text{m}$ disappears after centrifugation, which is most obvious in coal SH-B (Fig. 5), indicating that macropores $> 1 \mu\text{m}$ have a certain connectivity even though they are not abundant.

The continuity between the peaks of 0.02–1.0 ms and 2.0–25 ms, 2.0–25 ms and 25–500 ms of coal YW-B are weak, while that of coal YW-V is almost discontinuous (Fig. 5). This result shows that the connectivity between the pores of the Yuwu coal samples is poor, which also causes the characteristics of the T_2 spectra at S_w and S_{ir} . The T_2 spectra at S_{ir} for coal YW-B are significantly lower than those at S_w in the range of 0.02–1.0 ms due to the good connectivity of pores with widths of 10–300 nm. The T_2 spectra at S_{ir} for coal YW-B in the range of 2.0–25 ms and 25–500 ms move to the smaller pores, indicating that saturated water is centrifuged from pores corresponding to the peak of 0.02–1.0 ms and accumulates in pores corresponding to 2.0–6.0 ms. Macropores $> 1 \mu\text{m}$ and microfissures in coal YW-B have connectivity, and the saturated water in pores corresponding to the peaks of 2–25 ms and 25–500 ms is

centrifuged. The T_2 spectra at S_{ir} for coal YW-B in the range of 25–500 ms almost disappeared, indicating that microfissures and cleats have good connectivity. In summary, pores and fractures in coal YW-B have the greatest connectivity among the coal samples. The T_2 spectra at S_{ir} for coal YW-V in the range of 25–500 ms almost disappeared, while the other 3 peaks disappeared compared to the T_2 spectra at S_w . This result indicates that the connectivity of coal YW-V is extremely poor, and only the microfissures and cleats had connectivity.

3.3.3 Connectivity of the pores and fractures by X-ray CT

NMR has a low resolution of macropores $> 1 \mu\text{m}$. Therefore, the connectivity of pores and fractures at the micron-scale is further studied based on the X-ray CT results. Pore coordination numbers based on the X-ray CT results can quantitatively express pore connectivity (Lindquist et al. 2000; Sok et al. 2002). Figure 6 shows that the pore connectivity of coal SH-B is significantly better than that of coal SH-V, and the number of pores in each coordination number is larger than that in coal SH-V. The number of pores with a coordination number of 0 in coal YW-B and coal YW-V is basically the same, whereas the number of pores with a coordination number > 1 in coal YW-B is substantially larger than that in coal YW-V. Moreover, the coordination number of interconnected pores in coal SH-B is primarily 1–2, followed by 3–5, while the coordination number of pores in coal YW-B is slightly higher, which is mainly 5–6, followed by 3–4 (Fig. 6). However, there are almost no interconnected pores in coal SH-V and coal YW-V according to the coordination number (Fig. 6), indicating that the coal connectivity is extremely poor perpendicular to the bedding plane.

4 Discussion

4.1 Comparison of pore-fracture types

4.1.1 Morphology of pores and fractures identified by FESEM and X-ray CT images

Comparing the FESEM photographs (Fig. 7) and the X-ray CT images (Fig. 8), three main categories of pores and microscopic fractures are present in the coal samples, i.e., pores in the matrix (Figs. 7a, b; 8b, e), mineral-related pores (Figs. 7b, c; 8a) and microscopic fractures (Fig. 8c, d).

A. Pores in the matrix

The pores in the matrix develop in the coal organic matter and merge to form clusters with poor connectivity. These pores generally form irregular ellipses, and the long axes of the elliptical pores are directionally oriented due to paleotectonic stress (Figs. 7a, b; 8b, e). The pore widths of these

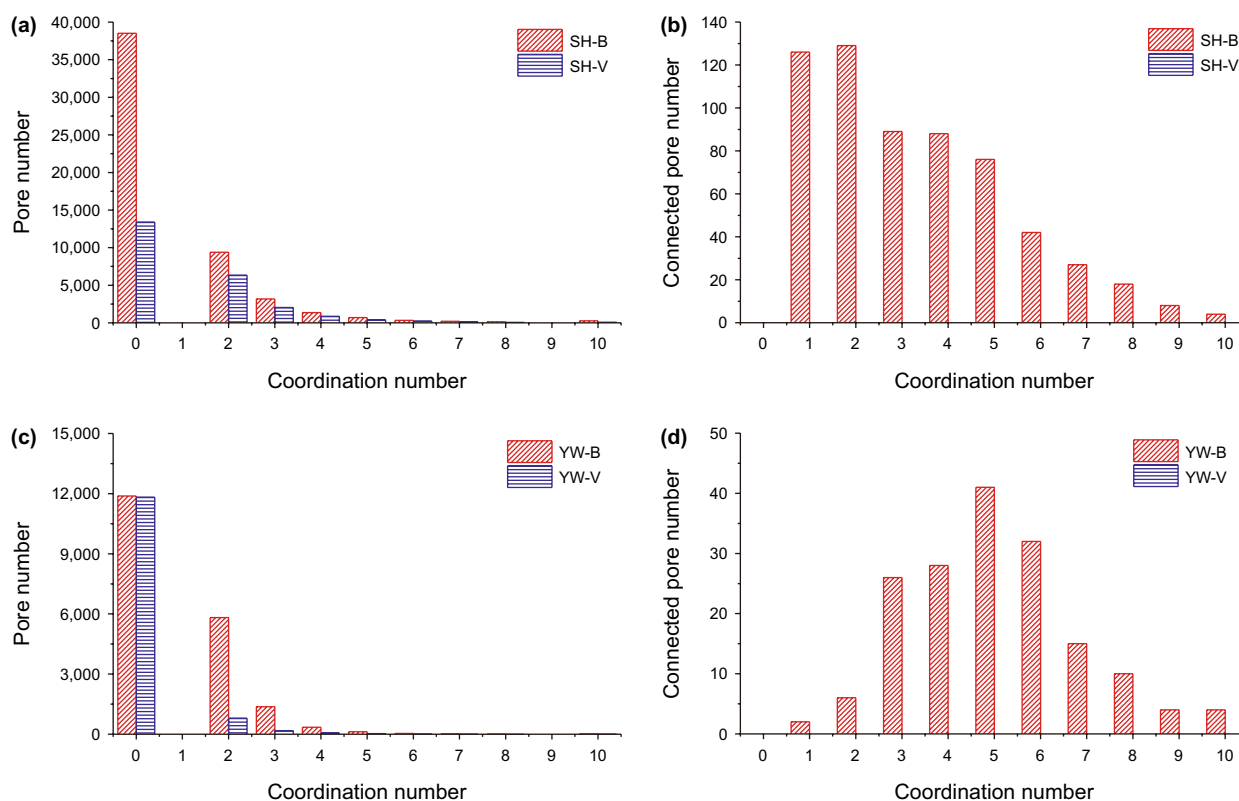


Fig. 6 Coordination number of pores and interconnected pores of the coal samples based on X-ray CT. *Notes:* **a, c** Coordination number of all pores in Sihe and Yuwu coal samples, respectively; **b, d** coordination number of interconnected pores in Sihe and Yuwu coal samples, respectively

pores are usually $< 5 \mu\text{m}$ and mainly 50–500 nm (Figs. 7a, b; 8b, e). These pores correspond to the peaks located at 0.2–5.0 ms (Sihe Mine) and 0.02–1.0 ms (Yuwu Mine) in the T_2 spectra at S_w and are major contributors to pores 1–5 μm in width according to X-ray CT. Based on the morphology, the pores in the matrix are mainly secondary gas pores.

B. Mineral-related pores

Mineral-related pores are formed around or in minerals and merge to form clusters with good connectivity (Figs. 7b, c; 8a). Some of these pores connect to each other to form a larger “hole” (Fig. 7c). Mineral-related pores do not have a fixed shape but are usually in the form of irregular elliptic and linear shapes and are also directionally oriented by the long axis (Figs. 7b; 8a). The pore size distribution of mineral-related pores is wide from mesopores to macropores. The pore widths of these pores are usually $< 20 \mu\text{m}$ and mainly 50–500 nm and 1–10 μm (Figs. 7b; 8a). Mineral-related pores are abundant in the coal samples, correspond to the peaks located at 0.01–0.2 ms, 0.2–5.0 ms (Sihe Mine) and 0.02–1.0 ms (Yuwu Mine) in the T_2 spectra at S_w and are major contributors to pores 1–20 μm in width according to X-ray CT. Based on the morphology and distribution area, these pores are mainly shrinkage-induced pores

around minerals and pores in minerals, with more abundant shrinkage-induced pores.

C. Microscopic fractures

The microscopic fractures in the coal samples are mainly macropore-scale, and some of the fractures are mesopore-scale. They are “pores” $> 50 \mu\text{m}$ according to the T_2 spectra and X-ray CT. Microscopic fractures with mesopores and macropores 50–500 nm in width are mainly linear shrinkage-induced pores (Fig. 7d). Microscopic fractures with widths $> 50 \mu\text{m}$ can be both cleats (C in Fig. 8) and microfissures (Fig. 8d). Cleats are typical endogenous fractures, and they are formed by the combined compaction, dehydration and contraction of devolatilization of the gelification materials during coalification (Liu et al. 2015). There are two groups of predominant cleat directions that are nearly orthotropic, e.g., face cleats and butt cleats. The cleats have good connectivity, and their widths are between a dozen micrometers and dozens of micrometers. The cleats are mostly closed or filled by minerals, which reduces the connectivity (Fig. 8c). The microfissures are relatively narrow (50–10 μm in width) and generally short (less than 1 mm in length), curved and dense without directionality (Fig. 8d). Although the microfissures have good connectivity, they are also filled by minerals, which reduces the connectivity and

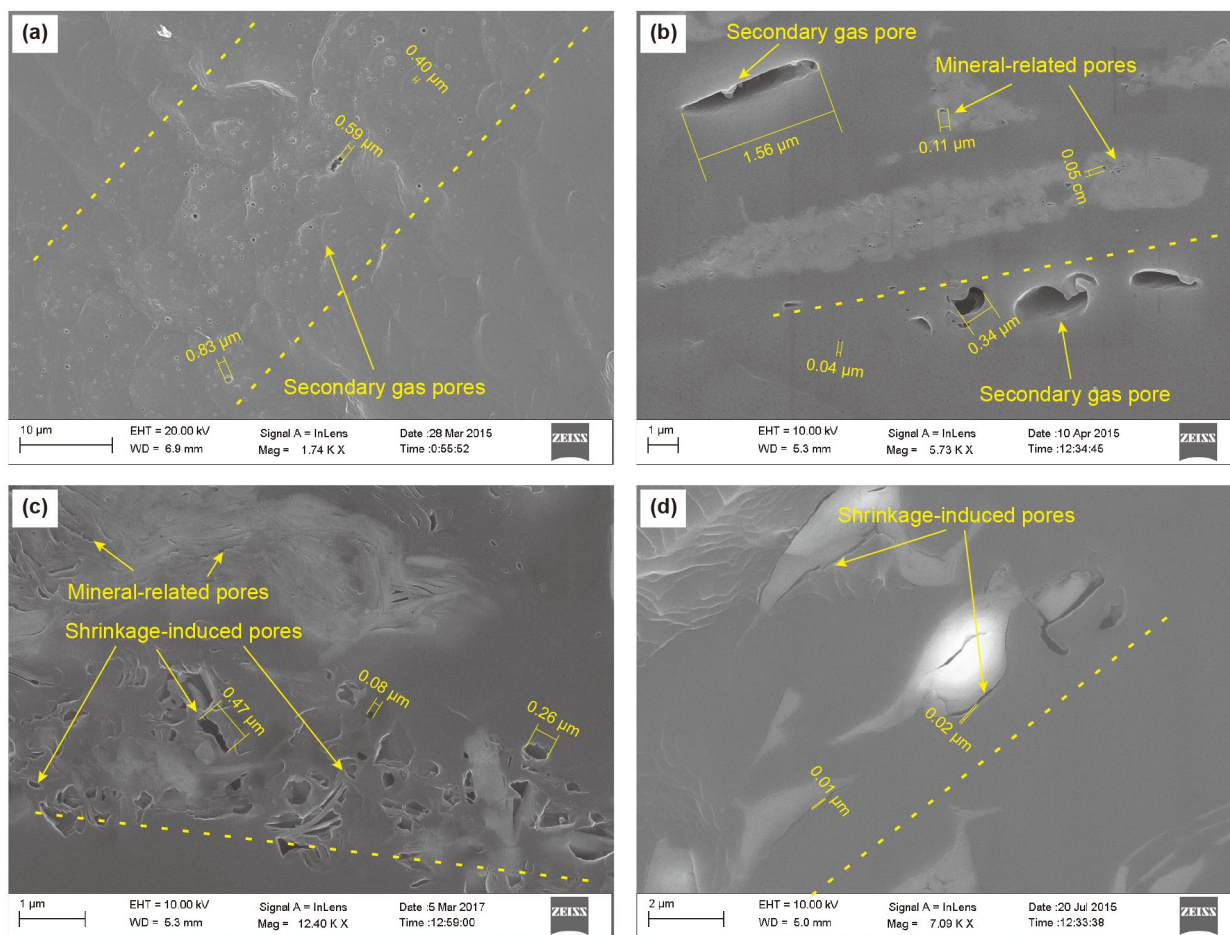


Fig. 7 Pores and fractures in coal samples based on FESEM. *Notes:* **a** Secondary gas pores in organic matter, Yuwu Mine; **b** secondary gas pores in organic and mineral-related pores in minerals, Yuwu Mine; **c** mineral-related pores in minerals and shrinkage-induced pores around minerals, Sihe Mine; and **d** shrinkage-induced pores around minerals, Sihe Mine

is the main reason for the lack of microscopic fracture peaks in the T_2 spectra at S_w in the Sihe coal samples (Fig. 8d).

4.1.2 Influence of pore-fracture types on connectivity

The 3D digital model and pore model show that coal SH-B is dominated by pores with few microscopic fractures, while coal SH-V has a large number of pores and microscopic fractures (Figs. 8; 9a, b). The abundant microscopic fractures result in a large volume of macropores $> 50 \mu\text{m}$, as shown in Fig. 4. Opposite to the Sihe coal samples, the pores and microscopic fractures in coal YW-B are more abundant than those in coal YW-V. The interconnected pore models show that coal SH-B and coal YW-B have connectivity, while the coal connectivity is extremely poor perpendicular to the bedding plane (Fig. 9c). That is identical with coordination number of interconnected pores shown in Fig. 6. Coal SH-B and coal YW-B have significantly different connectivity modes. Coal SH-B samples are mainly connected by

pores, while microscopic fractures are not abundant. Therefore, coal SH-B has mainly “pore connectivity,” where the throats are mainly pores, with single connecting channels and low coordination numbers. The coal YW-B are connected by microfissures, while the pores are not abundant in coal YW-B, and the connected area in coal YW-B is actually a microfissure with pores around it. Therefore, coal YW-B has “microfissure connectivity,” and the microfissures are the main channels connecting the pores, with more complicated connecting path.

4.2 Comparing with the throats of coal samples

The connectivity of coal samples indicates that throats are the key of coal connectivity, and the main reasons for the difference in the coal sample connectivity parallel and perpendicular to the bedding plane.

Figures 6b and 10 show that the number, width and length of throats in coal SH-B are larger than those in

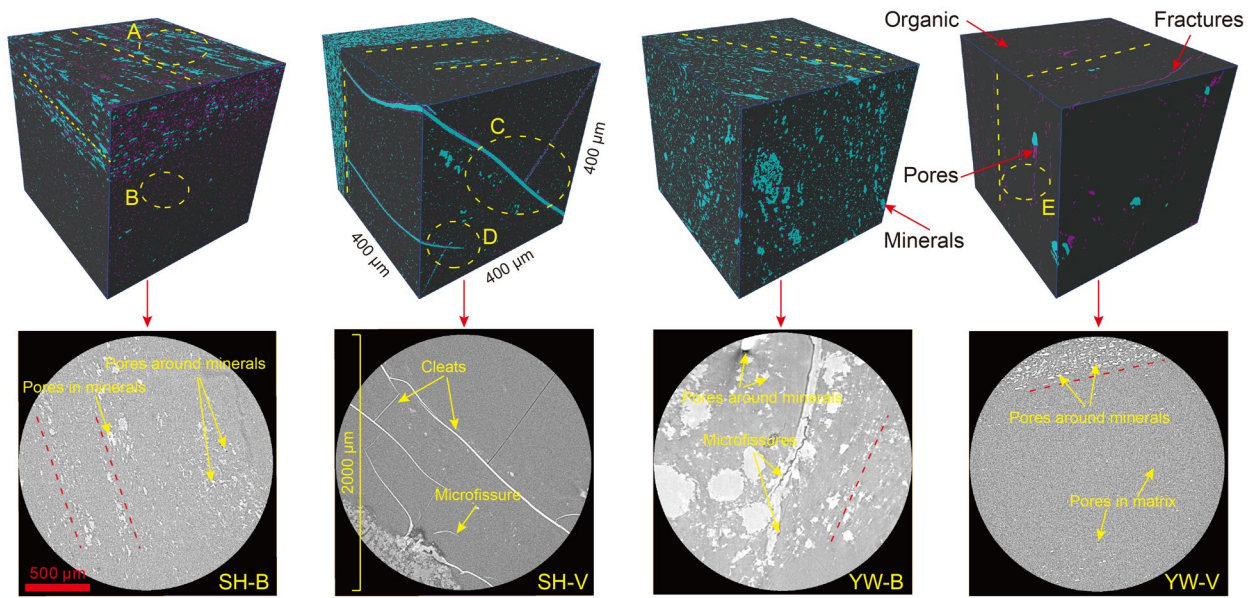


Fig. 8 3D digital model of coal samples based on X-ray CT. *Notes:* In the cubes, pores and fractures are carmine, minerals are blue, and organic matter is gray. In the X-ray CT images, pores and fractures are black, minerals are white and organic matter is light gray

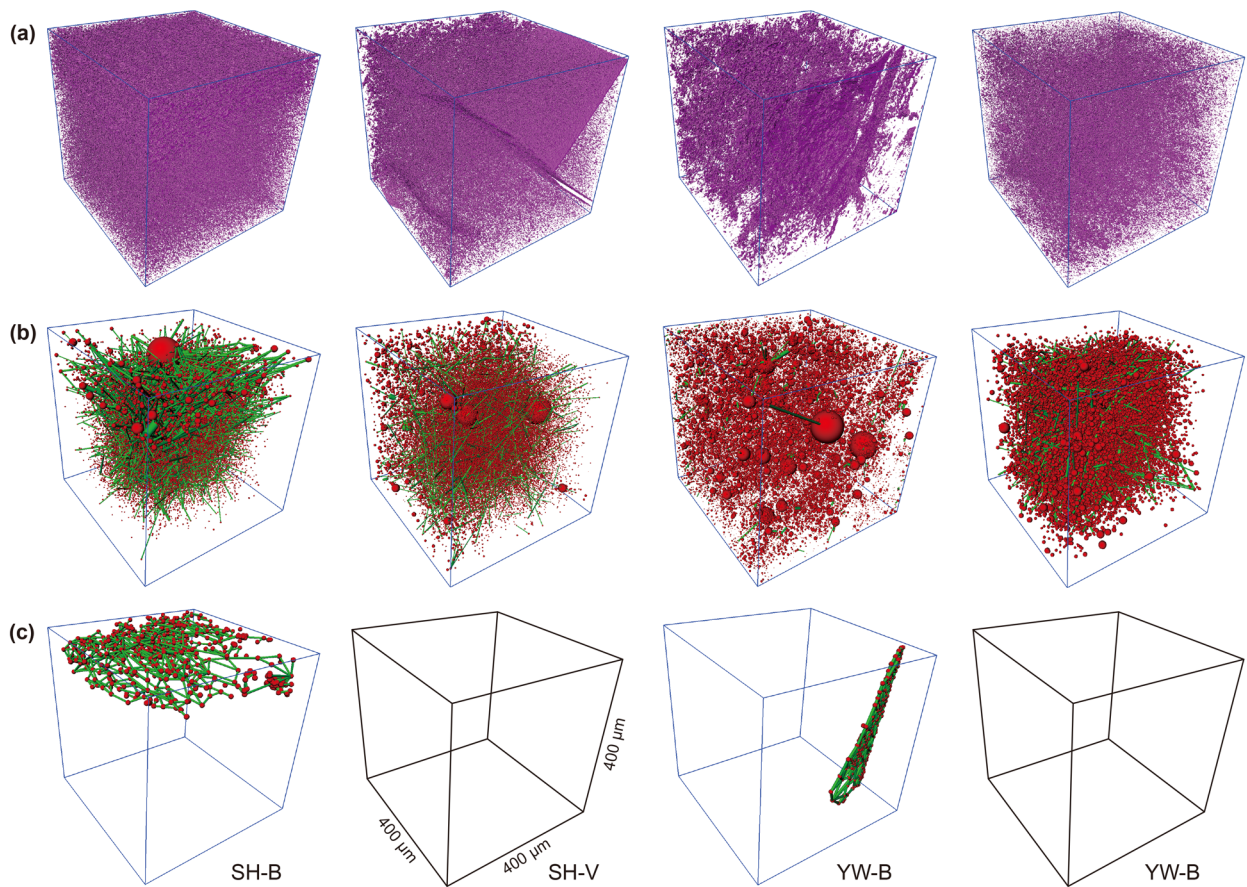


Fig. 9 Pore model and interconnected pore model of coal samples based on X-ray CT. *Notes:* **a** Pore models; **b** skeleton models of pores and throats; and **c** interconnected pore models. In the skeleton models and interconnected pore models, the pores are red, and the throats are green

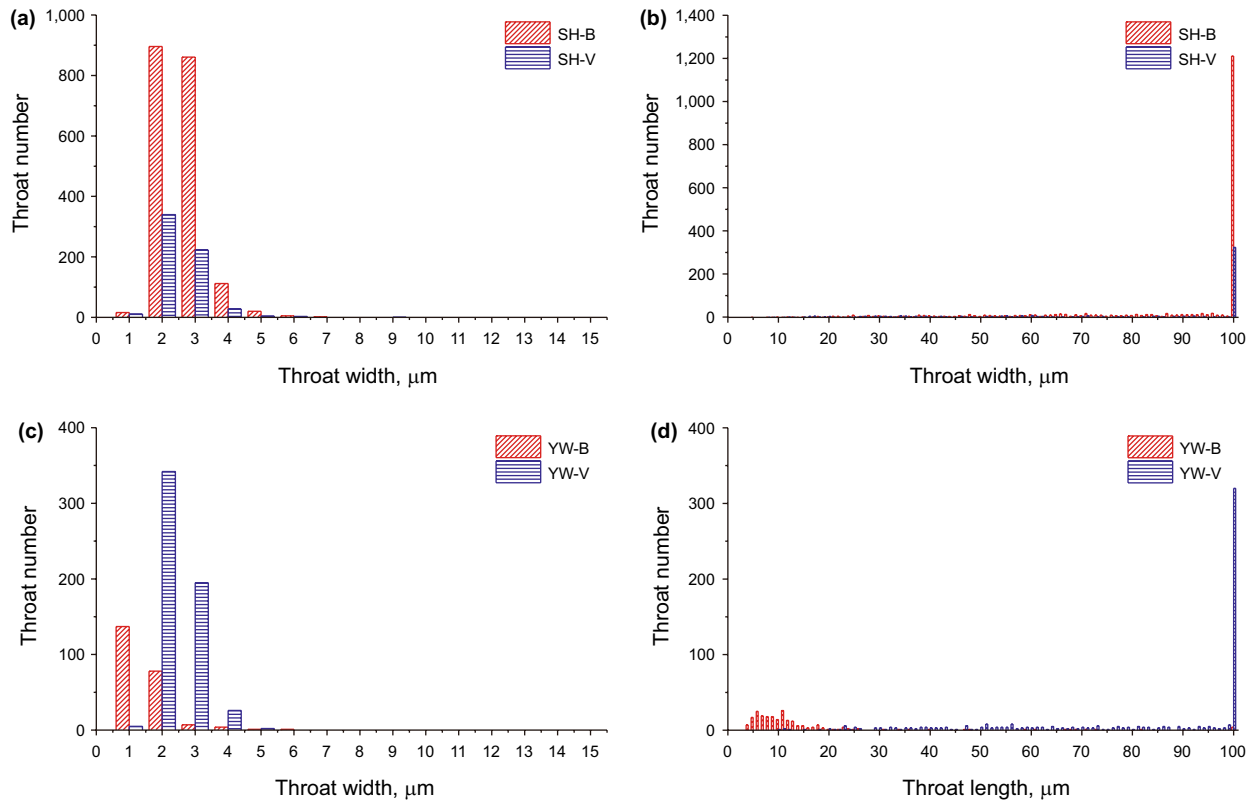


Fig. 10 Throat widths and lengths of the coal samples based on X-ray CT

coal SH-V, which is the main reason for the better connectivity in coal SH-B. The throat width of the Sihe coal samples is mainly 2–3 μm and is consistent with the pore width (Fig. 10), which further confirms that the throats of the Sihe coal samples are mainly pores. However, the 3D digital models (Fig. 8) and interconnected pore models (Fig. 9) show that the connectivity between cleats and pores, microscopic fractures and pores in coal SH-B is weak, and the throats in coal SH-B are mainly shrinkage-induced pores around minerals. Different from the Sihe coal samples, the number, width and length of throats in YW-B are smaller than those in coal YW-V (Figs. 6b, 10). The throats in coal YW-B are mainly microfissures, and the throat connectivity is determined by the connectivity between the microfissures and pores. However, the microfissures are not abundant in coal YW-V, and the throats in coal YW-V are mainly pores, resulting in the low coordination number of pores (0–1) (Fig. 6).

In conclusion, the pores are connected by throats, which determine the connectivity of high-rank coal. The contribution of microfissures to coal connectivity is superior to that of pores. Generally, microfissures are the main throats, which determine the coal connectivity.

Then, shrinkage-induced pores become the decisive factor of the pore connectivity when microfissures are not abundant.

4.3 Differences in spatial distribution of pores and fractures

4.3.1 Spatial distribution of pores on Coal SH-B

The pores, microscopic fractures and minerals are directionally oriented due to the influence of paleotectonic stress, forming a strip-like distribution in the coal samples (Figs. 7, 8). The orientations of the pores and minerals in the coal samples perpendicular to the bedding plane are significantly stronger than those of the samples parallel to the bedding plane (Fig. 8), indicating that the influence of the maximum and minimum horizontal principal stresses on the pore and mineral distributions is more significant than the vertical principal stress, causing the long axis of the pore to extend along the minimum horizontal principal stress. Due to the strip-like distribution of pores in coal SH-B, the pore connectivity is continuous parallel to the bedding plane (Fig. 11). Therefore, the pore connectivity

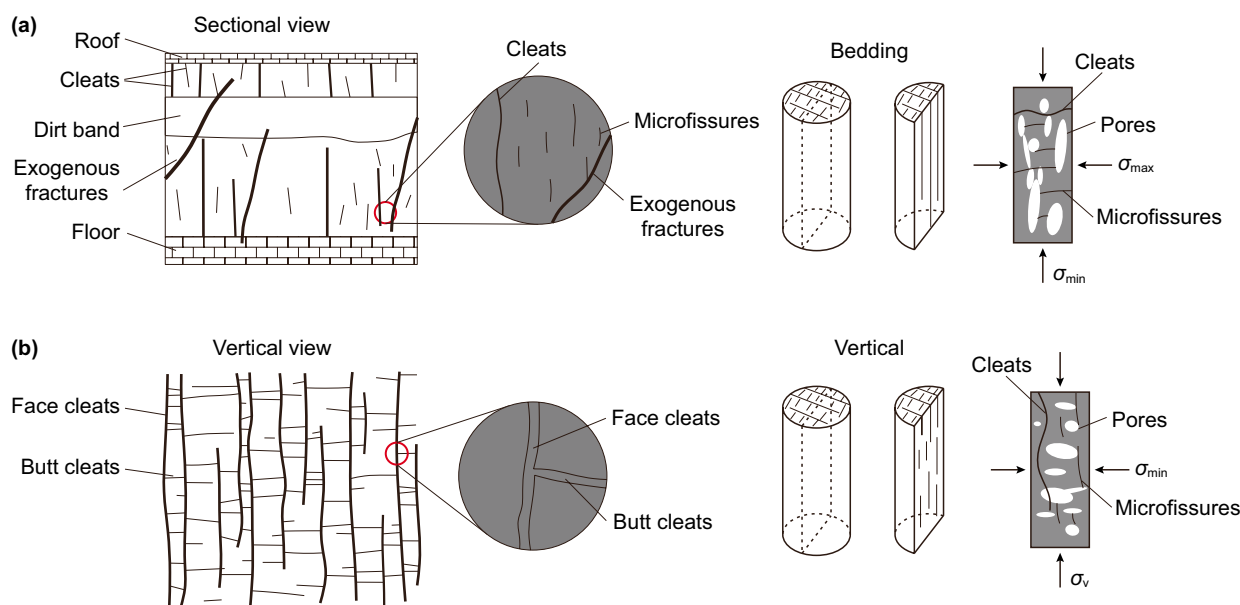


Fig. 11 Schematic diagram of the fractures in coal seam #3 in the southern Qinshui Basin (modified from Liu et al. 2018b). *Notes:* **a** Fractures parallel to the bedding plane; **b** fractures perpendicular to the bedding plane; σ_{\max} , maximum horizontal principal stress; σ_{\min} , minimum horizontal principal stress; σ_v , vertical principal stress

in the coal SH-B is better than the coal SH-V. It's important to note that microscopic fractures in coal SH-V are filled by minerals, which is an important factor for the poor connectivity of coal SH-V. We can assume that without mineral filling, the connectivity of coal SH-V may be better than coal SH-B, because that the contribution of microscopic fractures to coal connectivity is superior to that of pores.

4.3.2 Influence spatial distribution of fractures on connectivity

The cleats and microfissures of coal seam #3 in the southern Qinshui Basin are also directional and are usually perpendicular to or nearly perpendicular to the bedding and extend parallel to the bedding plane (Fig. 8). Therefore, the cleats and microfissures usually extend long distances parallel to the bedding plane, even throughout the coal pillar (Fig. 11a), which greatly improves the connectivity in the coal samples. These findings cause the effective porosity of coal YW-B to be comparable to that of coal SH-B or even better, although the NMR porosity and X-ray CT porosity of coal YW-B is only 1/2 of that of coal SH-B. Perpendicular to the bedding plane, the height of the cleats and microfissures in the coal samples are small and cannot intersect the coal pillar. In addition, the macropores are not abundant, and forming connections between the

cleats and microfissures is difficult (Fig. 11b), resulting in the extremely low connectivity of coal YW-V. In conclusion, the connectivity of the Yuwu coal samples is mainly dependent on the directionality of the microfissures.

5 Conclusions

In this paper, an integrated approach consisting of LF-NMR, X-ray CT, and FESEM was utilized to study the characteristics and causes of high-rank coal structure and connectivity parallel and perpendicular to the bedding plane. The following conclusions can be drawn from this study:

1. High-rank coal predominantly contains mesopores both parallel and perpendicular to the bedding plane, and the pore volume decreases with increasing pore width. Mesopores in high-rank coal are mainly shrinkage-induced pores and secondary gas pores. Due to the significant influence of the maximum horizontal principal stress, the morphology and spatial distribution of pores, fractures and minerals are strongly oriented perpendicular to the bedding plane.
2. The difference in the connectivity of high-rank coal is mainly due to the throat development and the orientation of pores and fractures. The pores extend along the minimum horizontal principal stress direction, while the

cleats and microfissures mainly extend parallel to the bedding plane, resulting the connectivity parallel to the bedding plane is significantly greater than that perpendicular to the bedding plane.

Acknowledgements This study was supported by the Fundamental Research Funds for the Central Universities (No. 2017XKQY017). We would like to thank engineers from the Shanxi CBM Branch of Huabei Oilfield Company and Lu'an Group and a number of research students, e.g., Shupei Liu, Xiong Ouyang, Jianguang Sun, and Kun Zhang from China University of Mining and Technology for their assistance in the coal sampling and some experiments.

Open Access This article is licensed under a Creative Commons Attribution 4.0 International License, which permits use, sharing, adaptation, distribution and reproduction in any medium or format, as long as you give appropriate credit to the original author(s) and the source, provide a link to the Creative Commons licence, and indicate if changes were made. The images or other third party material in this article are included in the article's Creative Commons licence, unless indicated otherwise in a credit line to the material. If material is not included in the article's Creative Commons licence and your intended use is not permitted by statutory regulation or exceeds the permitted use, you will need to obtain permission directly from the copyright holder. To view a copy of this licence, visit <http://creativecommons.org/licenses/by/4.0/>.

References

- Ai C, Li XX, Zhang J, et al. Experimental investigation of propagation mechanisms and fracture morphology for coalbed methane reservoirs. *Pet Sci*. 2018;15:815–29. <https://doi.org/10.1016/j.jngse.2009.03.003>.
- Alexeev AD, Feldman EP, Vasilenko TA. Methane desorption from a coal-bed. *Fuel*. 2007;86(16):2574–80. <https://doi.org/10.1016/j.fuel.2007.02.005>.
- Aminian K, Ameri S. Predicting production performance of CBM reservoirs. *J Nat Gas Sci Eng*. 2009;1(1–2):25–30.
- Bolin TB. S-XANES analysis of thermal iron sulfide transformations in a suite of Argonne Premium Coals: a study of particle size effects during pyrolysis. *Int J Coal Geol*. 2014;131:200–13. <https://doi.org/10.1016/j.coal.2014.06.015>.
- Chen Y, Tang DZ, Xu H, et al. Pore and fracture characteristics of different rank coals in the eastern margin of the Ordos Basin, China. *J Nat Gas Sci Eng*. 2015;26:1264–77. <https://doi.org/10.1016/j.jngse.2015.08.041>.
- Clarkson CR, Bustin RM. The effect of pore structure and gas pressure upon the transport properties of coal: a laboratory and modeling study. 2. Adsorption rate modeling. *Fuel*. 1999;78(11):1345–62. [https://doi.org/10.1016/S0016-2361\(99\)00056-3](https://doi.org/10.1016/S0016-2361(99)00056-3).
- Du ZG, Zhang XD, Huang Q, et al. The gas content distribution of coal reservoir at the Changzhi block, south-central Qinshui Basin, North China: influences of geologic structure and hydrogeology. *Energy Explor Exploit*. 2019;7(1):144–65. <https://doi.org/10.1177/0144598718784037>.
- Fang HH, Sang SX, Liu SQ. Numerical simulation of enhancing coalbed methane recovery by injecting CO₂ with heat injection. *Pet Sci*. 2019;16:32–43. <https://doi.org/10.1007/s12182-018-0291-5>.
- Hughes RG, Blunt MJ. Network modeling of multiphase flow in fractures. *Adv Water Resour*. 2001;24(3):409–21. [https://doi.org/10.1016/S0309-1708\(00\)00064-6](https://doi.org/10.1016/S0309-1708(00)00064-6).
- Keim SA, Luxbacher KD, Karmis M. A numerical study on optimization of multilateral horizontal wellbore patterns for coalbed methane production in Southern Shanxi Province, China. *Int J Coal Geol*. 2011;81(4):306–17. <https://doi.org/10.1016/j.coal.2011.03.004>.
- Knackstedt M, Arns C, Saadatfar M, et al. Virtual materials design: properties of cellular solids derived from 3D tomographic images. *Adv Eng Mater*. 2005;7(4):238–43. <https://doi.org/10.1002/adem.200400212>.
- Lai J, Wang GW, Fan ZY, et al. Insight into the pore structure of tight sandstones using NMR and HPMI measurements. *Energy Fuel*. 2016;30:10200–14. <https://doi.org/10.1021/acs.energyfuels.6b01982>.
- Lai J, Wang GW, Fan ZY, et al. Fracture detection in oil-based drilling mud using a combination of borehole image and sonic logs. *Mar Pet Geol*. 2017;84:195–214. <https://doi.org/10.1016/j.marpetgeo.2017.03.035>.
- Lai J, Wang GW, Wang ZY, et al. A review on pore structure characterization in tight sandstones. *Earth Sci Rev*. 2018;177:436–57. <https://doi.org/10.1016/j.earscirev.2017.12.003>.
- Li Y, Tang DZ, Elsworth D, et al. Characterization of coalbed methane reservoirs at multiple length scales: a cross-section from southeastern ordos basin, China. *Energy Fuel*. 2014;28(9):5587–95. <https://doi.org/10.1021/ef500449s>.
- Li Y, Zhang C, Tang DZ, et al. Coal pore size distributions controlled by the coalification process: an experimental study of coals from the Junggar, Ordos and Qinshui basins in China. *Fuel*. 2017;206:352–63. <https://doi.org/10.1016/j.fuel.2017.06.028>.
- Li PP, Zhang XD, Zhang S. Structures and fractal characteristics of pores in low volatile bituminous deformed coals by low-temperature N₂ adsorption after different solvents treatments. *Fuel*. 2018;224:661–75. <https://doi.org/10.1016/j.fuel.2018.03.067>.
- Li Y, Wang ZS, Pan ZJ, et al. Pore structure and its fractal dimensions of transitional shale: a cross-section from east margin of the Ordos basin, China. *Fuel*. 2019;241:417–31. <https://doi.org/10.1016/j.fuel.2018.12.066>.
- Lindquist WB, Venkatarangan A, Dunsmuir J, et al. Pore and throat size distributions measured from synchrotron X-ray tomographic images of Fontainebleau sandstones. *J Geophys Res*. 2000;105(B9):21509–27. <https://doi.org/10.1029/2000jb900208>.
- Liu SQ, Sang SX, Liu HH, et al. Growth characteristics and genetic types of pores and fractures in a high-rank coal reservoir of the southern Qinshui basin. *Ore Geol Rev*. 2015;64:140–51. <https://doi.org/10.1016/j.oregeorev.2014.06.018>.
- Liu SQ, Sang SX, Pan ZJ, et al. Study of characteristics and formation stages of macroscopic natural fractures in coal seam #3 for CBM development in the east Qinnan block, Southern Quishui Basin, China. *J Nat Gas Sci Eng*. 2016;34:1321–32. <https://doi.org/10.1016/j.jngse.2016.08.010>.
- Liu SQ, Sang SX, Wang G, et al. FIB-SEM and X-ray CT characterization of interconnected pores in high-rank coal formed from regional metamorphism. *J Pet Sci Eng*. 2017;148:21–31. <https://doi.org/10.1016/j.petrol.2016.10.006>.
- Liu SQ, Ma JS, Sang SX, et al. The effects of supercritical CO₂ on mesopore and macropore structure in bituminous and anthracite coal. *Fuel*. 2018a;223:32–43. <https://doi.org/10.1016/j.fuel.2018.03.036>.
- Liu SQ, Sang SX, Yang YH, et al. Structure features of high rank coal in parallel bedding and vertical bedding direction based on low field nuclear magnetic resonance (in Chinese). *Coal Sci Technol*. 2018b;46(10):110–6. <https://doi.org/10.13199/j.cnki.cst.2018.10.017>.
- Ma JS, Couples GD, Jiang ZY, et al. A multi-scale framework for digital core analysis of gas shale at millimeter scales. In: *The*

- unconventional resources technology conference, 25–27 August, Denver; 2014a. <https://doi.org/10.15530/urtec-2014-1934450>.
- Ma JS, Sanchez JP, Wu K, et al. A pore network model for simulating non-ideal gas flow in micro- and nano-porous materials. *Fuel*. 2014;116:498–508. <https://doi.org/10.1016/j.fuel.2013.08.041>.
- Mathews JP, Pone JDN, Mitchell GD, et al. High-resolution X-ray computed tomography observations of the thermal drying of lump-sized subbituminous coal. *Fuel Process Technol*. 2011;92(1):58–64. <https://doi.org/10.1016/j.fuproc.2010.08.020>.
- Moore TA. Coalbed methane: a review. *Int J Coal Geol*. 2012;101:36–81. <https://doi.org/10.1016/j.coal.2012.05.011>.
- Okolo GN, Everson RC, Neomagus HWJP, et al. Comparing the porosity and surface areas of coal as measured by gas adsorption, mercury intrusion and SAXS techniques. *Fuel*. 2015;141:293–304. <https://doi.org/10.1016/j.fuel.2014.10.046>.
- Smolná K, Gregor T, Kosek J. Morphological analysis of high-impact polypropylene using X-ray micro CT and AFM. *Eur Polym J*. 2013;49(12):3966–76. <https://doi.org/10.1016/j.eurpolymj.2013.08.030>.
- Sok RM, Knackstedt MA, Sheppard AP, et al. Direct and stochastic generation of network models from tomographic images; effect of topology on residual saturations. *Transp Porous Med*. 2002;46(2):345–71. <https://doi.org/10.1023/a:1015034924371>.
- Wei C, Qin Y, Wang GGX, et al. Simulation study on evolution of coalbed methane reservoir in Qinshui basin, China. *Int J Coal Geol*. 2007;72(1):53–69. <https://doi.org/10.1016/j.coal.2006.12.001>.
- Wen GJ, Liu W, Xu C, et al. Automated hydraulic correction technology for CBM horizontal wellbore. *Int J Coal Geol*. 2011;85(2):191–201. <https://doi.org/10.1016/j.coal.2010.07.007>.
- Yao YB, Liu DM. Comparison of low-field NMR and mercury intrusion porosimetry in characterizing pore size distributions of coals. *Fuel*. 2012;95:152–8. <https://doi.org/10.1016/j.fuel.2011.12.039>.
- Yao YB, Liu DM, Che Y, et al. Petrophysical characterization of coals by low-field nuclear magnetic resonance (NMR). *Fuel*. 2010a;89(7):1371–80. <https://doi.org/10.1016/j.fuel.2009.11.005>.
- Yao YB, Liu DM, Cai YD, et al. Advanced characterization of pores and fractures in coals by nuclear magnetic resonance and X-ray computed tomography. *Sci China Earth Sci*. 2010b;53(6):854–62. <https://doi.org/10.1007/s11430-010-0057-4>.
- Yao YB, Liu DM, Xie SB. Quantitative characterization of methane adsorption on coal using a low-field NMR relaxation method. *Int J Coal Geol*. 2014;131:32–40. <https://doi.org/10.1016/j.coal.2014.06.001>.
- Zhang SH, Tang SH, Tang DZ, et al. The characteristics of coal reservoir pores and coal facies in Liulin district, Hedong coal field of China. *Int J Coal Geol*. 2010;81(2):117–27. <https://doi.org/10.1016/j.coal.2009.11.007>.
- Zhang XD, Du ZG, Li PP. Physical characteristics of high-rank coal reservoirs in different coal-body structures and the mechanism of coalbed methane production. *Sci China Earth Sci*. 2017;60(2):246–55. <https://doi.org/10.1007/s11430-016-5178-y>.
- Zhang XD, Zhang S, Li PP, et al. Investigation on solubility of multicomponents from semi-anthracite coal and its effect on coal structure by Fourier transform infrared spectroscopy and X-ray diffraction. *Fuel Process Technol*. 2018;174:123–31. <https://doi.org/10.1016/j.fuproc.2018.02.018>.
- Zhao YX, Sun YF, Liu SM, et al. Pore structure characterization of coal by NMR cryoporometry. *Fuel*. 2017;190:359–69. <https://doi.org/10.1016/j.fuel.2016.10.121>.
- Zhou HW, Zhong JC, Ren WG, et al. Characterization of pore-fracture networks and their evolution at various measurement scales in coal samples using X-ray μ CT and a fractal method. *Int J Coal Geol*. 2018;189:35–49. <https://doi.org/10.1016/j.coal.2018.02.007>.
- Zhu JF, Liu JZ, Yang YM, et al. Fractal characteristics of pore structures in 13 coal specimens: relationship among fractal dimension, pore structure parameter, and slurry ability of coal. *Fuel Process Technol*. 2016;149:256–67. <https://doi.org/10.1016/j.fuproc.2016.04.026>.